Title

Effect of Pitch Attitude on the Performance and Acoustics of a Lift-Offset Coaxial Rotor Based on High-Fidelity CFD/CSD Simulations

Journal

Proceedings of the Vertical Flight Society 75th Annual Forum and Technology Display

Authors

Jia, Zhongqi
Sharma, Kalki
Lee, Seongkyu
et al.

Publication Date

2019-05-13

DOI

10.4050/f-0075-2019-14451

Effect of Pitch Attitude on the Performance and Acoustics of a Lift-Offset Coaxial Rotor Based on High-Fidelity CFD/CSD Simulations

Zhongqi Jia
Ph.D. Student

Seongkyu Lee
Assistant Professor

Department of Mechanical and Aerospace Engineering
University of California, Davis
Davis, California, 95616 U.S.A.

Kalki Sharma
Ph.D. Student

Kenneth S. Brentner
Professor

Department of Aerospace Engineering
The Pennsylvania State University
University Park, Pennsylvania, 16802 U.S.A.

ABSTRACT

This paper investigates the effect of pitch attitude on both performance and acoustics of a lift-offset coaxial rotor based on a first-principles and high-fidelity CFD/CSD loose coupling approach at 150 and 200 knots. The pitch attitudes selected for this research are -5°, 0°, and 5°. The CFD/CSD loose coupling simulations are carried out using the CREATE™-AV software Helios while the coaxial rotor acoustics is simulated using PSU-WOPWOP at eight microphones positioned below the lower rotor. A detailed aerodynamic analysis is performed at 150 knots. A total of six major aerodynamic interactions are identified: 1) hub-wake interaction, 2) self-BVI, 3) parallel rotor-to-rotor BVI, 4) blade-crossover events, 5) root-induced BVI, and 6) reversed-flow-edge-vortex interactions. The strength of these interactions is dependent on the vehicle pitch attitude. The cases with negative pitch attitude show significantly stronger impulsive pressure pulses, which is found to be induced by parallel rotor-to-rotor BVIs of the lower rotor. Moreover, the positive and zero pitch attitude cases tend to dominate the acoustic region on the starboard side of the coaxial rotor, whereas the negative pitch attitude case shows higher acoustic pressure peaks on the port side. Overall, the case with a positive pitch attitude shows significant improvement in rotor aerodynamic efficiency, rotor acoustics, and vehicle power performance at high speed. The hemispherical acoustic simulation results at 150 knots also show that the noise is less likely to propagate in the forward direction with a positive pitch attitude.

NOTATION

α	pitch attitude of the vehicle, deg
c_∞	speed of sound in the undisturbed medium, m/s
C_{tip}	tip chord length, m
C_p	pressure coefficient, $(p-p_\infty)/(.5\rho_\infty c_\infty^2)$
d	distance to the nearest wall, m
D	rotor drag force in the wind-axis direction, N [or lbf]
D_e	effective drag, N [or lbf]
F_z	blade sectional normal force, N/m
$dF_z/d\Omega$	azimuthal (time) derivative of F_z, N/(m-deg)
LO	lift offset of the coaxial rotor
$\vec{l}$	blade surface loading vector, N/m
l_r	$\vec{l}\cdot\hat{r}$, N/m
L	rotor lift, N [or lbf]
L_{ref}	grid unit reference length, m [or ft]
mid-frequency SPL	the logarithmic summation of SPLs between 10th and 50th harmonics, dB
$\vec{M}$	local Mach number vector
M_∞	freestream Mach number
M_r	$\vec{M}\cdot\hat{r}$
M_{AT}	advancing tip Mach number
p	fluid pressure, Pa
p_∞	ambient pressure, Pa
p'	total acoustic pressure, Pa
p'_L	loading noise acoustic pressure, Pa
p'_T	thickness noise acoustic pressure, Pa
P_{total}	total power of the vehicle, hp

Presented at the Vertical Flight Society 75th Annual Forum & Technology Display, Philadelphia, Pennsylvania, May 13–16, 2019.

P_{upper}	upper rotor power, hp
P_{lower}	lower rotor power, hp
q	q-criterion, $\frac{1}{2}(\|\|W_{ij}\|\|^2 - \|\|S_{ij}\|\|^2)$, 1/s^2
$\bar{q}$	non-scaled q-criterion, $q/(c_\infty/L_{ref})^2$
R	rotor radius, m [or ft]
SPL	sound pressure level, dB
r	distance between $\vec{y}$ and $\vec{x}$, m
$\hat{r}$	unit vector in the radiation direction
r_p	radial position of the blade, m [or ft]
r_b	nondimensional radial position, r_p/R
S_{ij}	strain-rate tensor, 1/s^2
SPL	sound pressure level, dB
t	observer time, s
T	total rotor thrust, N [or lbf]
T_{aux}	auxiliary engine thrust, N [or lbf]
u^*	friction velocity, $= \sqrt{\tau_w/\rho_\infty}$, m/s
v	local fluid velocity on the blade surface, m/s
V_∞	freestream velocity, knots [m/s or ft/s]
W_{ij}	spin-rate tensor, 1/s^2
$\vec{x}$	observer location, m
y^+	dimensionless wall distance, $u^* d/\nu$
$\vec{y}$	acoustic source location, m
ρ_∞	air density, kg/m^3
μ	advance ratio
ν	air viscosity, m^2/s
τ_w	wall shear stress, N/m^2
Ω	rotor rotation rate, RPM
η	propeller propulsive efficiency
Ψ	rotor azimuth, deg
ΔM_x	differential rolling moment, N-m [or lbf-ft]

Acronyms

ABC	Advancing Blade Concept
BVI	blade-vortex interaction
CFD	computational fluid dynamics
CSD	computational structural dynamics
CCW	counterclockwise
CW	clockwise

Subscript

ret	at retarded time

Superscript

$\circ$	deg

INTRODUCTION

High-speed flight capability is an essential requirement of modern military rotorcraft. In 2009, the United States Secretary of Defense established the Future Vertical Lift (FVL) initiative, a plan to replace the current fleet with a new family of helicopters, which can attain better flight performance (e.g. higher flight speed) than the aging helicopters (Ref. 1). One of the barriers of high-speed helicopter designs is retreating blade stall, a well-known rotorcraft aerodynamic phenomenon: the retreating side of the rotor disk can no longer generate additional integrated lift to balance the rolling moment induced by the advancing side of the rotor disk. The Sikorsky Aircraft Corporation, a Lockheed Martin Company, together with the Boeing Company are currently developing a coaxial compound helicopter, the SB>1 Defiant™ JMR (Joint Multi-Role) Technology Demonstrator as shown in Fig. 1 (Ref. 2), based on the Advanced Blade Concept (ABC) (Ref. 3) for the Army's Joint Multi-Role Technology Demonstration program, the precursor of FVL.

Fig. 1: A conceptual drawing of the Boeing/Lockheed Martin SB>1 Defiant™ (Ref. 2).

Fig. 2: The Sikorsky XH-59A (Ref. 4).

The ABC rotor design has been demonstrated on the XH-59A, which is shown in Fig. 2 (Ref. 4), by the Sikorsky Aircraft Corporation in the late 1960s to mitigate the adverse effect of retreating blade stall. The main motivation of the ABC rotor design is to fully exploit the lift potential of a coaxial rotor by utilizing the lift capability of the advancing side of the rotor while avoiding retreating blade stall on the retreating side of the rotor. This strategy also results in each rotor carrying a rolling moment of equal magnitude and opposite direction due to the lift being offset toward the advancing side of the rotor. The mathematical expression of lift offset (LO) can be written as:

$$\mathrm{LO} = \frac{\Delta M_x}{T \cdot R} \tag{1}$$

where ΔM_x is the differential rolling moment between the upper and lower rotors, T is the total rotor thrust, and R is the rotor radius.

Unlike a conventional helicopter, most modern coaxial rotorcraft designs have featured an auxiliary propulsion system. For instance, the XH-59A has two turbojet engines positioned on the sides of the fuselage that produce the forward thrust. Such a vehicle is no longer required to tilt the main rotor forward for propulsive thrust, and the rotor is not required to operate at a single nominal rotational speed, which could significantly impact power, performance, and acoustics.

Previous research (Refs. 6–8) has also shown various advantages of a lift-offset coaxial rotor on lift capacity and power performance. The Sikorsky Corporation has demonstrated that the X2 Technology™ Demonstrator, a lift-offset coaxial configuration with a pusher propeller, can attain better flight performance at a speed above 120 knots at a positive pitch attitude ranging from 2° to 5° (Ref. 5). Additionally, Herman et al. (Ref. 9) performed a detailed multidisciplinary trim analysis on a four-bladed lift-offset coaxial configuration with a pusher propeller using a low-fidelity rotorcraft comprehensive analysis code. Their research suggested that the total power, a sum of rotor and pusher propeller power, can be minimized by operating the vehicle at a positive pitch attitude around 5° at speeds ranging from 150 to 260 knots. The paper also showed that the total noise of the coaxial configuration was reduced with a slightly positive pitch attitude at high speed.

Although a lift-offset coaxial rotor can achieve satisfactory high-speed flight performance, it is susceptible to significant impulsive noise. Walsh et al. (Ref. 10) performed acoustic analysis of a three-bladed lift-offset coaxial rotor based on the low-fidelity simulation software: Rotorcraft Comprehensive Analysis System (RCAS) (Ref. 11). They have identified blade-vortex interaction (BVI) noise-like pressure pulses, which are induced by interactions between the blade-tip vortices and blade surfaces in close proximity. Their research also suggested that the acoustics of a coaxial rotor can be reduced and controlled by manipulating pilot control parameters, such as rotor rotation rate. Furthermore, Kim et al. (Ref. 12) analyzed the acoustics of a two-bladed lift-offset coaxial rotor based on a medium-fidelity Vorticity Transport Model (VTM) developed by Brown (Ref. 13). They have identified rotor-to-rotor BVI at an advance ratio of 0.24 due to the close interaction between tip vortices of one rotor and blades of the other rotor. They also demonstrated that the tip vortex of rotor-to-rotor BVI is parallel with respect to the blade span, which can lead to highly impulsive noise. In addition to BVI noise, Barbely et al. (Ref. 14) found abrupt change of blade surface pressure when two blades crossover, which is another impulsive acoustic source of a coaxial rotor, based on 2D CFD (Computational Fluid Dynamics) simulations of a two-bladed coaxial rotor.

In 2018, Jia et al. (Refs. 15, 16) performed a series of acoustic studies on a notional XH-59A coaxial rotor with lift offset based on high-fidelity CFD/CSD (Computational Structural Dynamics) simulations. The pitch attitude of the vehicle was fixed at zero degrees. Their results showed that both self-BVI (tip vortex interaction with the same rotor) and blade-crossover interactions are dominant acoustic sources of a lift-offset coaxial rotor at high speed. The blade-crossover interactions, which are induced by the pressure interaction between the upper and lower rotor blades, were found to increase dramatically in strength with increasing flight speed and lift offset. The acoustics of the coaxial rotor is sensitive to the lift-offset value, but less influenced by the vertical separation distance between the upper and lower rotors at high speed.

Although the acoustics of a lift-offset coaxial rotor has been studied in recent years, none of the previous studies has investigated the impact of pitch attitude, a pilot control parameter, on the acoustics of a lift-offset coaxial rotor based on high-fidelity simulations. The main focus of this paper is to investigate the acoustic characteristics of a lift-offset coaxial rotor under the influence of pitch attitude based on a first-principles and high-fidelity CFD/CSD loose coupling approach at high speed. A notional coaxial rotor hub geometry is incorporated in the CFD model in order to assess the effect of the rotor hub on acoustics. Both strength and origin of acoustic sources are analyzed thoroughly. It is anticipated that rotor-to-rotor BVI events would occur due to a variation of pitch attitude. Moreover, the impact of pitch attitude on acoustic directivity is also investigated. The correlation between vehicle power, rotor aerodynamic efficiency, and rotor acoustics is determined and will serve as a reference guide to minimize vehicle power and rotor noise.

METHOD

A three-bladed hingeless coaxial model — the XH-59A — with stiff composite blades is chosen based on the publicly available technical report written by Ruddell (Ref. 17). Some of the aircraft properties of the XH-59A are shown in Table 1. Since the airfoil data of the XH-59A are not publicly available, airfoils that match with the thickness distribution of the actual airfoils are used: NACA-0026 is used for r_b (nondimensional radial position) < 0.42; NACA-63216 is used for $0.42 \leq r_b \leq 0.68$; NACA-23012 is used for $r_b > 0.68$. Blade chord, thickness, and twist distributions are shown in Fig. 3. A linear distribution of blade chord, thickness, and twist is assumed between 10% and 20% span.

Table 1: Basic Properties of the XH-59A.

Aircraft Length	12.7 m (41.67 ft)
Aircraft Height	2.4 m (8 ft)
Rotor Radius	5.5 m (18 ft)
Number of Rotors	2
Blades per Rotor	3
Upper Rotor Rotation	CCW
Lower Rotor Rotation	CW
Vertical Separation Distance	0.76 m (2.5 ft)
Shaft Tilt Angle	0°
Nominal Rotor Speed	345 RPM
Nominal Rotor Tip Speed	198 m/s (650 ft/s)
Gross Weight	5,398 kg (11,900 lb)
Power Plants (Lift)	Two PT6-3
Power Plants (Auxiliary Thrust)	Two J60-P3A

A notional XH-59A hub with radius equal to 0.09 rotor radius (R) is incorporated in the XH-59A model based on a 2D hub sketch of Ruddell's report (Ref. 17), which is different from the earlier studies (Refs. 15, 16). The root section of the XH-59A blade is also extended inward from 20% to 10% span in order to reduce the impact of vorticies generated by blade roots on acoustics. Figure 4 shows a comparison between the

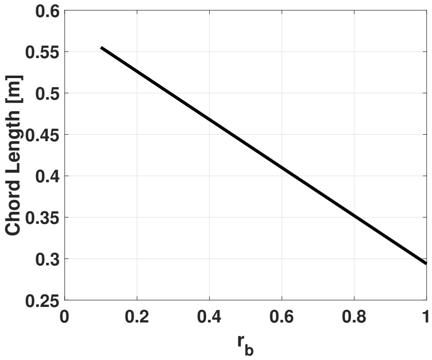

(a) Blade chord distribution.

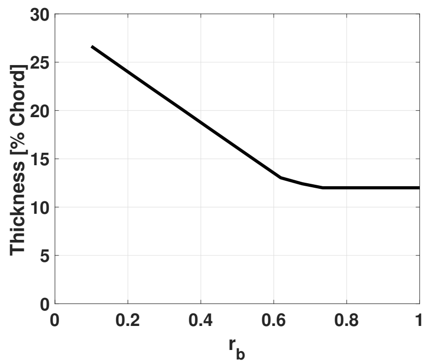

(b) Blade thickness distribution.

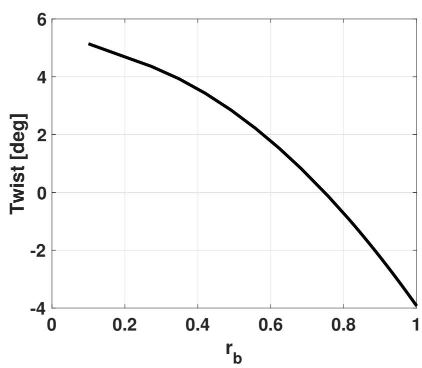

(c) Blade twist distribution.

Fig. 3: Rotor Blade Properties of the XH-59A.

hub and hubless models with a single blade from the top view. A tiny gap is left between the rotor hub and each rotor blade to allow the change of blade motions. The upper hub, lower hub, and shaft fairings are combined as one component and assumed stationary.

CFD Mesh

A dual-mesh paradigm, dividing the computational domain into near-body overset mesh and off-body Cartesian mesh, is implemented in the present work. NASA's structured overset grid generation software Chimera Grid Tools (CGT) (Ref. 18) is used for the generation of near-body grids based on an O-grid topology (see Fig. 5a). Figure 6 shows the entire model. Each blade is composed of three components: main blade,

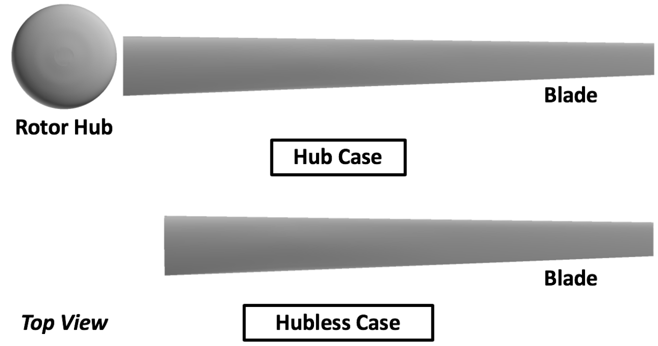

Fig. 4: Hub model vs. hubless model.

blade root, and blade tip. Both grid dimension and spacing of the main blade for the hub and hubless cases are maintained to be the same for acoustic comparison. The dimensions of the main blade are 267 (chordwise) $\times$ 189 (spanwise) $\times$ 65 (normal) grid points with leading and trailing edge spacings equal to 0.05% C_{tip} and 0.02% C_{tip} respectively, where C_{tip} is the tip chord length. The dimensions of the root- and tip-cap grids are 125 $\times$ 121 $\times$ 65 points and 128 $\times$ 121 $\times$ 65 points, respectively. The dimensions of the main hub grid are 201 $\times$ 129 $\times$ 65 points. The distance of the near-body grids in the normal direction is 1.0 C_{tip} with a wall spacing equal to 5.0 $\times$ 10^{-4}% C_{tip}, which is computed based on a dimensionless wall distance $y^+ = 1.0$. The end spacing in the normal direction is 10% C_{tip} and matches with the finest wake-grid spacing of the Cartesian mesh.

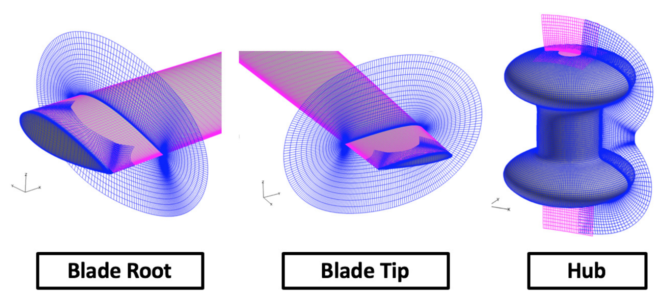

(a) The near-body grids.

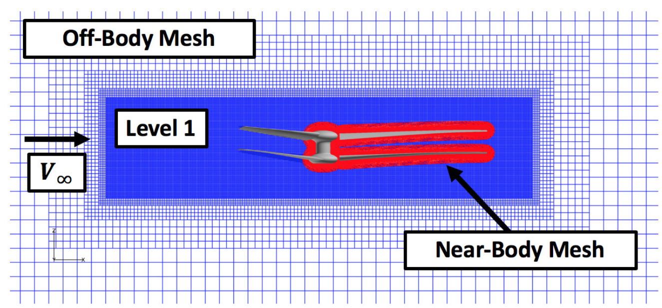

(b) The Cartesian mesh.

Fig. 5: Near- and off-body meshes.

The total number of grid points per blade is approximately 5.2 million, and 31.2 million for all six blades. The total number

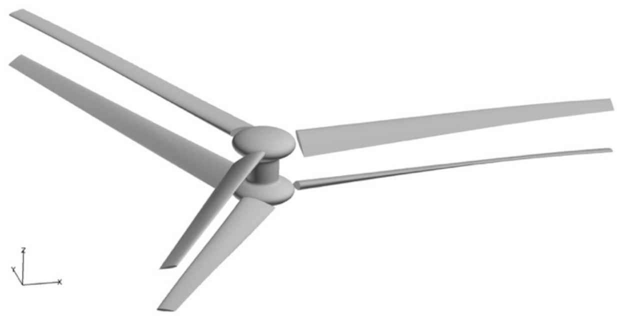

Fig. 6: The entire configuration.

of grid points of the hub is approximately 1.8 million. The outer boundaries of the off-body Cartesian mesh (see Fig. 5b) are 20 rotor radii away from the origin in each direction. The off-body mesh has approximately 130 million grid points after numerical convergence. Eight levels of Adaptive Mesh Refinement (AMR) with the finest wake-grid spacing (Level 1) equal to 10% C_{tip} are used after the first rotor revolution in order to better capture the rotor-wake interaction.

CFD/CSD Loose Coupling Setup

CFD/CSD loose coupling simulations are achieved using the high-fidelity rotorcraft simulation and comprehensive analysis software Helios (Ref. 19), which is being developed under the U.S. Department of Defense (DoD) Computational Research and Engineering Acquisition Tools and Environments - Air Vehicles (CREATE^{TM}-AV) program. The vehicle is trimmed using RCAS, the CSD and flight dynamics module of Helios that is also capable of predicting structural deformation. The vertical force is trimmed to balance the weight of the vehicle by the pilot collective pitch of both upper and rotors. The net rotor torque, rolling moment, and pitching moment are trimmed by the pilot differential collective, lateral cyclic, and longitudinal cyclic pitches, respectively. The differential rolling and pitching moments are trimmed by differential pilot lateral and longitudinal cyclic pitches. The rotor lift offset defined in Eq. (1) is achieved by trimming the differential rolling moment of both upper and lower rotors to a desired value. The force equilibrium in the x-direction is achieved by balancing the rotor drag, rotor propulsive force, auxiliary propulsion thrust, and fuselage drag. The fuselage drag coefficient used in this work is estimated based on the experiment conducted by Felker (Ref. 20) in the 40- by 80-foot wind tunnel at NASA Ames.

Following the rotorcraft trim analysis, the CFD setup of this research is established. The structured-grid compressible near-body solver OVERFLOW (Ref. 21) and the adaptive Cartesian off-body solver SAMCart (Ref. 22) of Helios are used for flow simulations. A fifth-order spatial scheme and a second-order temporal scheme are used for time-accurate CFD simulations in both near- and off-bodies. The turbulence model used in this research is the Spalart-Allmaras RANS turbulence model (Ref. 23) coupled with Detached Eddy Simulation (Ref. 24). A time step size of 0.25 degrees azimuth which results in 1,440 time steps per rotor revolution is used. 40 and 10 dual-time-stepping subiterations within each physical time step are performed for temporal convergence in the near- and off-body simulations, respectively. The frequency of loose coupling simulation is set to be every 180 degrees azimuth after the first rotor revolution. A detailed description of the CFD/CSD loose coupling process is given by Potsdam et al. (Ref. 25). Blade surface solutions are extracted at every 0.5 degrees azimuth or every two time steps over the last rotor revolution for acoustic prediction.

Acoustic Simulation Setup

Acoustic simulations are performed using PSU-WOPWOP (Refs. 26, 27), which is being developed at the Pennsylvania State University that has very general capabilities and can accept input data of varying fidelities. PSU-WOPWOP utilizes a numerical implementation of Farassat's Formulation 1A (Refs. 28, 29) of the Ffowcs Williams and Hawkings (FW-H) equation (Ref. 30). An impermeable surface strategy, which only considers blade surface loading, is used for acoustic prediction in this work, and the quadrupole source term of the FW-H equation is neglected. The equations of Farassat's Formulation 1A can be written:

$$p'(\vec{x},t) = p'_T(\vec{x},t) + p'_L(\vec{x},t) \tag{2}$$

$$\begin{aligned} 4\pi p'_T(\vec{x},t) = & \int_{f=0} \left[\frac{\rho_\infty(\dot{v}_n + v_{\dot{n}})}{r|1-M_r|^2}\right]_{ret} dS + \\ & \int_{f=0} \left[\frac{\rho_\infty v_n(r\dot{M}_r + c(M_r - M^2))}{r|1-M_r|^3}\right]_{ret} dS \end{aligned} \tag{3}$$

$$\begin{aligned} 4\pi p'_L(\vec{x},t) = & \frac{1}{c_\infty}\int_{f=0} \left[\frac{\dot{l}_r}{r|1-M_r|^2}\right]_{ret} dS + \\ & \int_{f=0} \left[\frac{l_r - l_M}{r^2|1-M_r|^2}\right]_{ret} dS + \\ & \frac{1}{c_\infty}\int_{f=0} \left[\frac{l_r(r\dot{M}_r + c(M_r - M^2))}{r^2|1-M_r|^3}\right]_{ret} dS \end{aligned} \tag{4}$$

In Eq. (3) and Eq. (4) of Farassat's Formulation 1A, there are two key terms which should be reviewed before the discussion of acoustic results. The first term is $1/|1-M_r|$, which is known as the Doppler amplification factor (Ref. 10). The Doppler amplification factor depends on both the magnitude of blade surface Mach number ($\vec{M}$) and the unit normal vector ($\hat{r}$). $\hat{r}$ is directly associated with the relative positions between rotor blades and observers. The Doppler amplification factor is expected to be high when an advancing blade with high surface Mach number moves toward an observer. The second term is $\dot{l}_r$ of Eq. (4). This term is directly proportional to the intensity of abrupt change of airloads. Impulsive aerodynamic interactions, such as BVI, can lead to a high value of $\dot{l}_r$, which ultimately yields impulsive loading noise. However, a combination of high $\dot{l}_r$ and low $1/|1-M_r|$ may not lead to impulsive noise. It should also be noted that the second and third integrals of Eq. (4), when compared to the first integral of Eq. (4), are generally smaller in magnitude in far-field acoustic prediction because of r^2 in the denominators. These two integrals are often considered as the near-field terms, and are only important in near-field acoustic prediction.

Microphone Positions

Eight microphones, each with a direct distance equal to approximately $5R$ from the mid point between the upper and lower rotors, are used to investigate the acoustics of the lift-offset coaxial rotor. Table 2 shows the position of each microphone in terms of rotor radius (R). These microphones are also positioned in a circular manner and $1R$ below the mid-point between the two hubs. Figure 7 shows a schematic representation of the microphone positions. Microphones 2, 3, and 4 are positioned on the port side of the coaxial rotor while microphones 6, 7, and 8 are positioned on the starboard side of the coaxial rotor.

Table 2: Microphone Positions (referenced from the mid point between the two rotor hubs).

Microphone Number	Position (x,y,z), R (R = 5.49 m)
1	(-5.00, 0.00, -1.00)
2	(-3.54, -3.54, -1.00)
3	(0.00, -5.00, -1.00)
4	(3.54, -3.54, -1.00)
5	(5.00, 0.00, -1.00)
6	(3.54, 3.54, -1.00)
7	(0.00, 5.00, -1.00)
8	(-3.45, 3.45, -1.00)

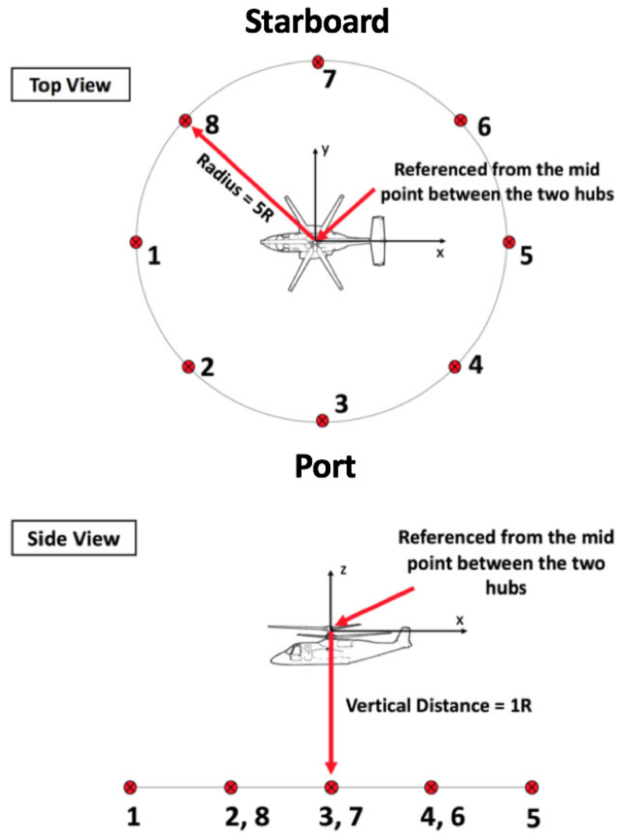

Fig. 7: A schematic representation of microphone locations.

RESULTS

Two speed cases (150 and 200 knots) with LO = 0.2 at an attitude of 3000 ft (914 m) are considered for this research. The three chosen pitch attitudes (α) are $-5°$, $0°$, and $5°$ for each speed case with the flight conditions specified in Table 3. The M_{AT} at 200 knots is kept the same as the M_{AT} at 150 knots by reducing the rotor rotation rate in order to avoid highly non-linear and compressible flow physics such as drag divergence and delocalization, which normally should be avoided if possible. The total power of the vehicle at 150 and 200 knots are validated against available flight test data in an earlier study conducted by Jia et al. (Ref. 15). Although the near-body unsteady residual has only dropped by a maximum of approximately 1.8 order, rotor forces and moments are converged after approximately 11 loose coupling iterations or six rotor revolutions.

Table 3: Flight conditions at 100, 150, and 200 knots.

Speed (knots)	M_∞	M_{AT}	μ	Ω (RPM)
150	0.23	0.82	0.39	345
200	0.30	0.82	0.59	300

Aerodynamic Interactions at 150 Knots

The effect of pitch attitude on acoustic sources is first investigated at 150 knots ($\mu = 0.39$) with LO = 0.2. Figure 8 shows the iso-surfaces of a non-scaled q-criterion ($\bar{q} = 0.001$) colored by vorticity magnitude and corresponding vorticity contour at Y = 0 with $\alpha = -5°$, $0°$, and $5°$. Significant hub-wake interaction is found near $\Psi = 0°$ of both upper and lower rotors. While both $\alpha = -5°$ and $0°$ cases show stronger hub-wake interaction on the lower rotor, the $\alpha = 5°$ case shows stronger interaction between the hub wake and the upper rotor. Self-BVI and blade-crossover events are also found from the iso-surfaces of the q-criterion. These blade-crossover events occur when the upper rotor blades overlap with the lower rotor blades. The self-BVI events located on the advancing side of each rotor are induced by interactions between the blade-tip vortices and blades of the same rotor in close proximity. These self-BVI events at $\alpha = 0°$ are expected to be stronger than the events shown at $\alpha = -5°$ and $5°$ due to a smaller separation distance between tip vortices and rotor blades.

Figure 9 shows a zoomed-in view of the iso-surface of q-criterion at $\alpha = 0°$. Both root-induced BVI and reversed-flow-edge vortex interactions are also found, and these interactions also occur at $\alpha = -5°$ and $5°$. Since the rotor blades are not concatenated with the rotor hub in the CFD model, root-induced BVI events are expected. However, the strength of these root-induced BVI events is greatly dissipated due to

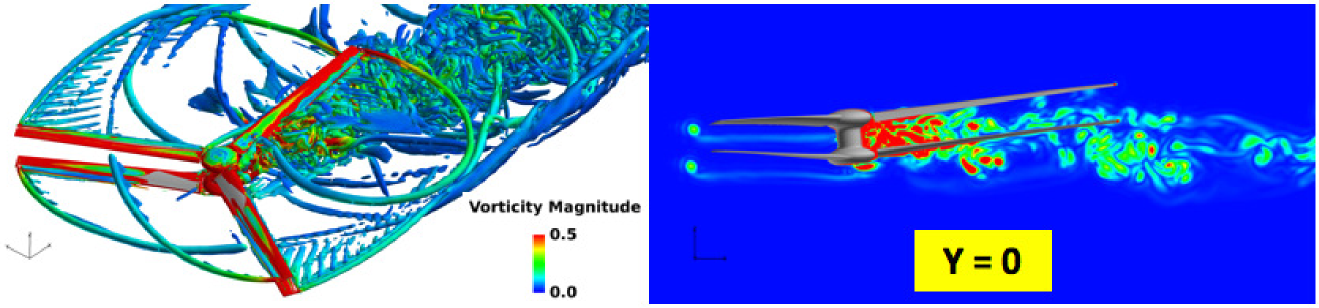

(a) $\alpha = -5°$.

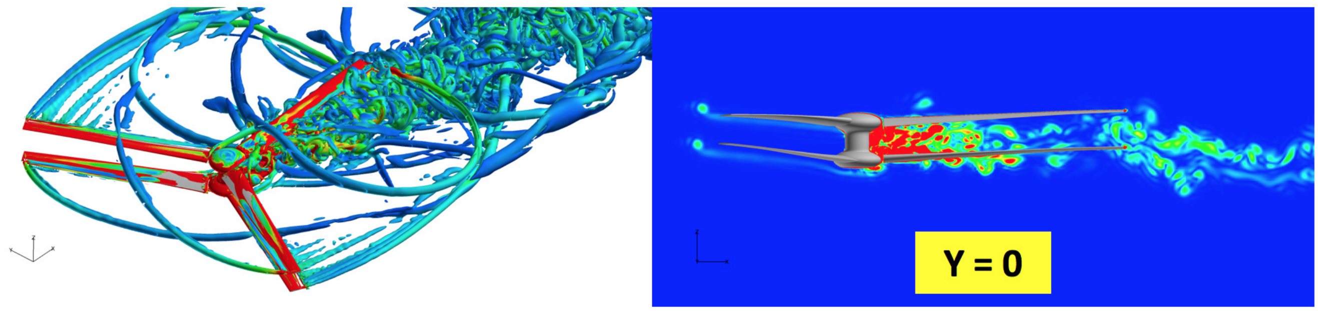

(b) $\alpha = 0°$.

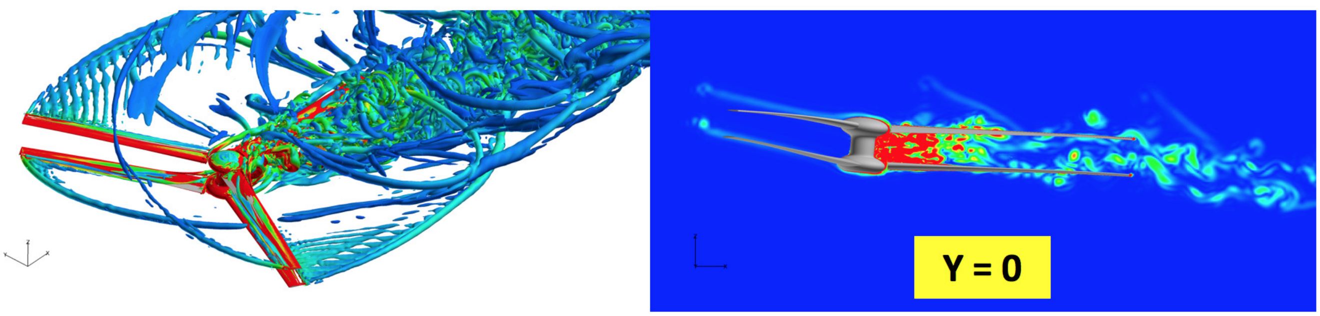

(c) $\alpha = 5°$.

Fig. 8: A comparison of vorticity contours at 150 knots.

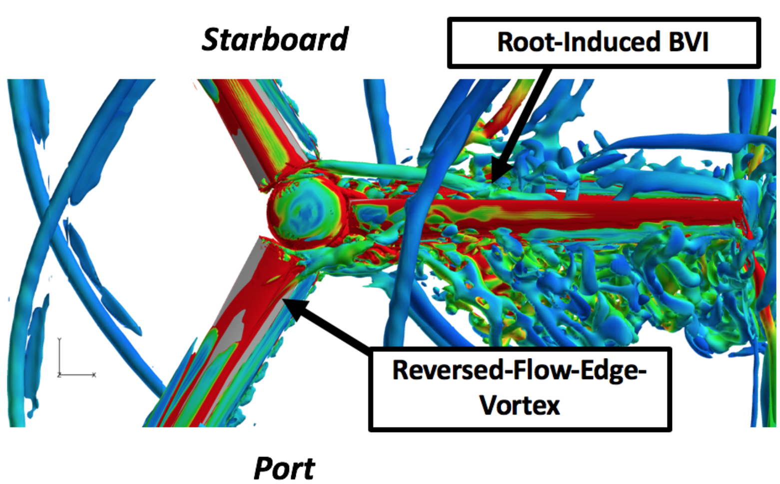

Fig. 9: Root-induced BVI and reversed-flow-edge-vortex interactions at 150 knots with $\alpha = 0°$.

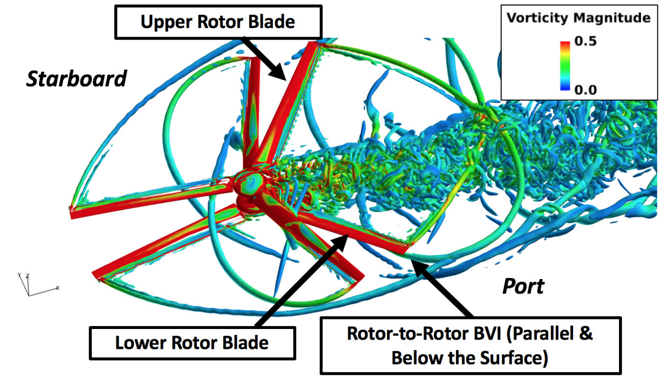

(a) $\Psi = 45^\circ$ of the lower rotor at $\alpha = -5^\circ$.

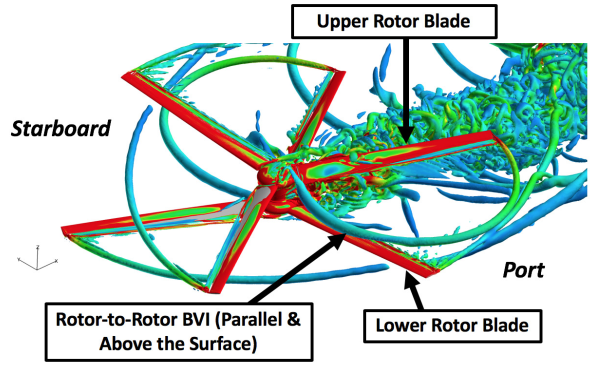

(b) $\Psi = 90^\circ$ of the lower rotor at $\alpha = -5^\circ$.

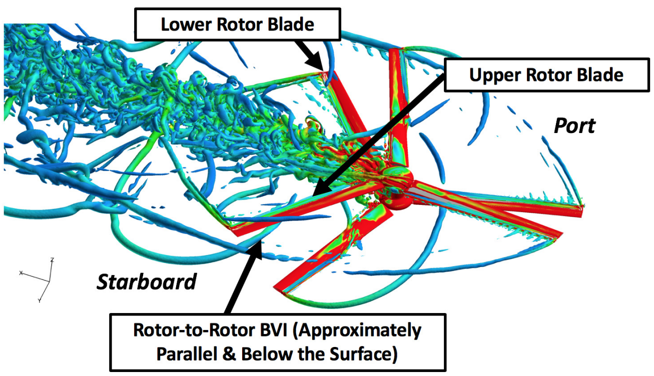

(c) $\Psi = 45^\circ$ of the upper rotor at $\alpha = 5^\circ$.

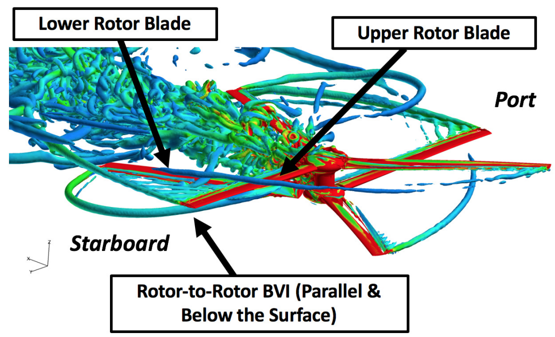

(d) $\Psi = 90^\circ$ of the upper rotor at $\alpha = 5^\circ$.

Fig. 10: Rotor-to-rotor BVIs at 150 knots.

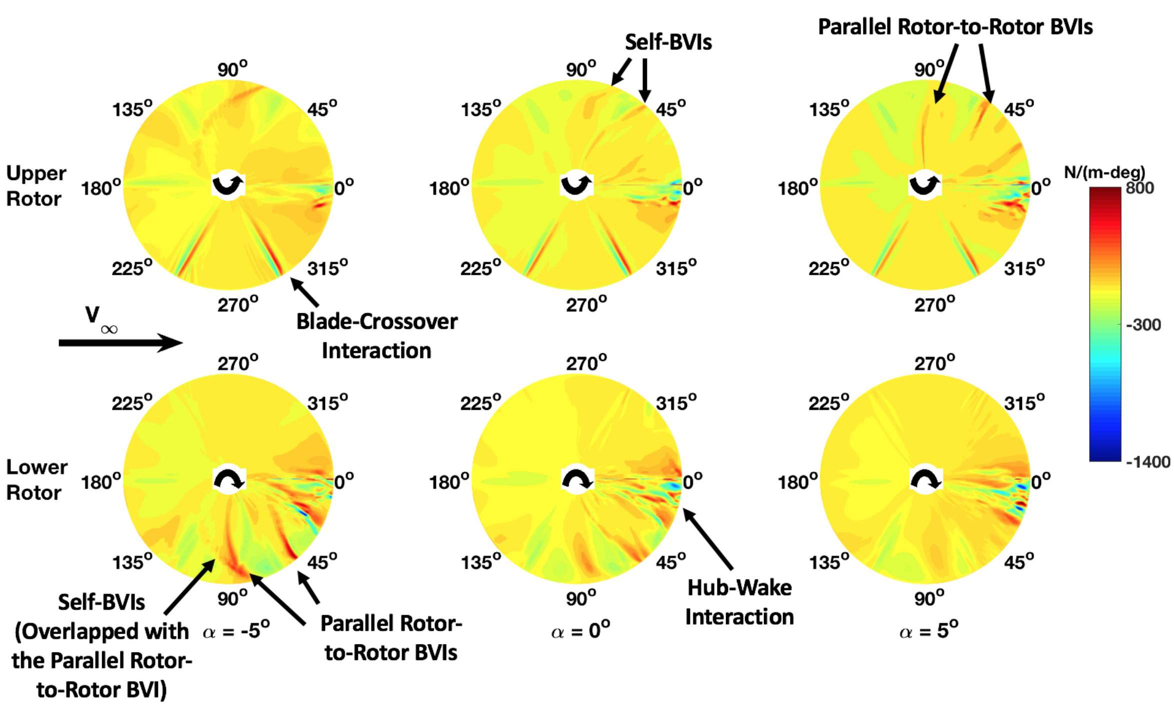

Fig. 11: The polar contours of $dF_z/d\Omega$ at 150 knots.

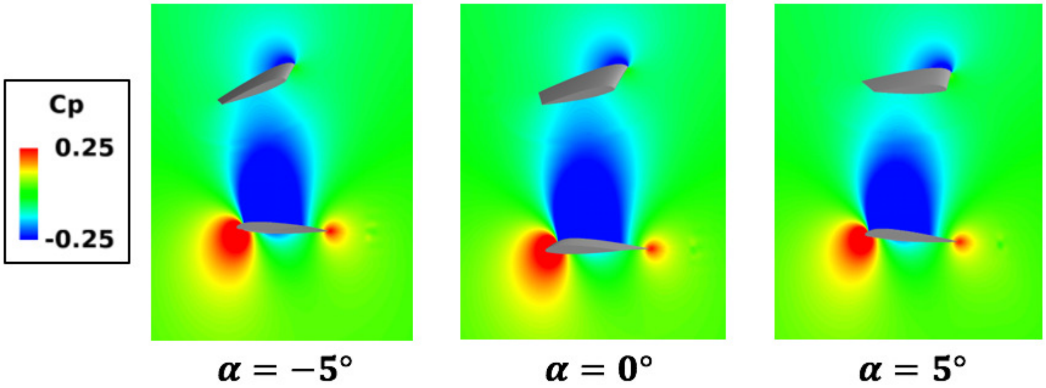

Fig. 12: A comparison of the blade-crossover event at $\Psi = 300°$ at 150 knots.

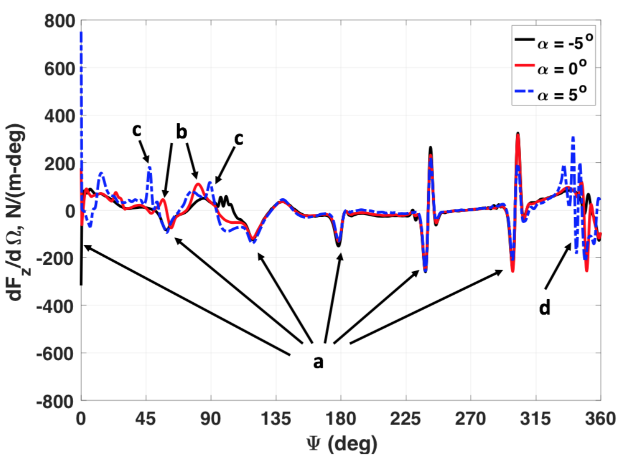

(a) Upper rotor.

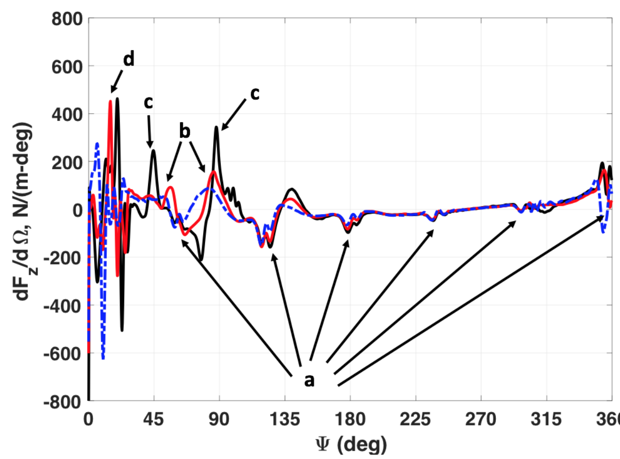

(b) Lower rotor.

Fig. 13: $dF_z/d\Omega$ at 75% span (a: blade-crossover events. b: self-BVIs. c: parallel rotor-to-rotor BVIs. d: hub-wake interaction.)

the viscous interaction of the hub. The reversed-flow-edge-vortex, which was also found by Potsdam et al. (Ref. 31) in high-speed rotor simulations, is shown in Fig. 9, which is induced by the flow separation at the leading edge in the reverse flow direction on the retreating blades of the upper rotor. This reversed-flow-edge vortex moves toward zero degrees of the rotor azimuthal angle. It should also be noted that both root-induced BVIs and reversed-flow-edge-vortices are merged together with the hub wake near $\Psi = 0°$, and additional turbulence is produced. Moreover, parallel rotor-to-rotor BVIs, which imply the parallel interaction between the tip vortices of one rotor and the blades of the other rotor, are identified at non-zero pitch attitudes: $\Psi = 45°$ (see Fig. 10a) and $\Psi = 90°$ (see Fig. 10b) of the lower rotor at $\alpha = -5°$; $\Psi = 45°$ (see Fig. 10c) and $\Psi = 90°$ (see Fig. 10d) of the upper rotor at $\alpha = 5°$. These parallel rotor-to-rotor BVI events are responsible for generating major impulsive noise.

The polar contours of the azimuthal derivative of sectional normal force ($dF_z/d\Omega$), which serve as an indicator of impulsive airloads and a direct source term in Farassat's Formulation 1A, are also plotted at $\alpha = -5°$, $0°$, and $5°$ (see Fig. 11) to further investigate the effect of pitch attitude on acoustic source. Some key aerodynamic events are highlighted in Fig. 11. The blade-crossover events, which occur at every 60 degrees rotor azimuth, starting at $\Psi = 0°$, are found on both upper and lower rotors in each case. As α increases from $-5°$ to $5°$, the strength of the blade-crossover event at $\Psi = 300°$ of the upper rotor is reduced (shown in a lighter red color) due to a reduction of pressure interaction between the upper and lower rotor blades as shown in Fig. 12. The blade-crossover event at $\Psi = 60°$ of the lower rotor is also reduced in magnitude (changing from green to light yellow) due to the same reason.

In addition to the blade-crossover events, the self-BVI events, which are also impulsive acoustic sources, are found at $\alpha = -5°$ and $0°$. While only one self-BVI event is noticeable near $\Psi = 80°$ on both upper and lower rotors at $\alpha = -5°$, two self-BVI events are identified near $\Psi = 50°$ and $\Psi = 80°$ of both upper and lower rotors at $\alpha = 0°$. Impulsive parallel rotor-to-rotor BVIs are also identified at the same locations as described in Fig. 10. These parallel rotor-to-rotor BVIs are significantly more impulsive at $\alpha = -5°$ than at $\alpha = 5°$. Hub-wake interactions, which are merged with root-induced BVIs and reversed-flow-edge-vortex interactions, are also found near $\Psi = 0°$. While the strength of the hub-wake interaction of the upper rotor is increased with increasing α, the intensity of the hub-wake interaction of the lower rotor is decreased as α increases.

In order to show a better quantitative comparison of the aerodynamic interactions, $dF_z/d\Omega$ at 75% span is plotted (see Fig. 13). The upper rotor results are first analyzed based on Fig. 13a. The magnitude of the blade-crossover event at $\Psi = 300°$ between the $\alpha = -5°$ and 0° cases is comparable. However, the magnitude of this interaction is reduced by 40% at $\alpha = 5°$. The maximum peak value of the parallel rotor-to-rotor BVI events at $\alpha = 5°$ is 70% higher than that of the self-BVI events at $\alpha = 0°$ and 5°. The hub-wake interaction is also significantly stronger at $\alpha = 5°$ than at $\alpha = -5°$ and 0°. The upper rotor of the $\alpha = 5°$ case, overall, is expected to show higher sound pressure level than the upper rotor of the other two cases at 150 knots.

On the lower rotor (see Fig. 13b), the $\alpha = -5°$ case shows significantly impulsive rotor-to-rotor BVI events. The maximum peak value of these events at $\alpha = -5°$ is approximately 2.3 times higher than the maximum peak value of the self-BVI events at $\alpha = -5°$. The rotor-to-rotor BVI events are also stronger than the blade-crossover events on the lower rotor. Additionally, the hub-wake interaction in the first quadrant of the lower rotor also shows dramatic turbulent interactions in all cases, but more intensive at $\alpha = -5°$ due to the root-induced BVI events of the upper rotor interacting with the lower rotor. Unlike the upper rotor trend, the $\alpha = -5°$ case, overall, shows stronger impulsive aerodynamic interactions.

Acoustics at 150 Knots

After identifying impulsive acoustic sources of the coaxial rotor at $\alpha = -5°$, 0°, and 5°, the effect of pitch attitude on rotor acoustics is investigated at 150 knots. Figure 14 shows the loading noise acoustic pressure as a function of observer time. The $\alpha = -5°$ case shows significantly higher acoustic pressure peaks at microphones 2, 3, and 4, which are positioned on the port side of the coaxial rotor. On the other hand, the $\alpha = 5°$ case shows slightly higher acoustic pressure peaks at microphones 6, 7, and 8, which are positioned on the starboard side of the coaxial rotor. Recall the discussion of the Doppler amplification factor under Acoustic Simulation Setup: the magnitude of this factor is dependent on both the magnitude of surface tip Mach number and the relative position between the microphone and noise source. The advancing side of each rotor, where the maximum blade-tip Mach number occurs, is considered as the major acoustic source area. A combination of strong Doppler amplification and abrupt change of airloads will likely yield impulsive acoustics. Since the parallel rotor-to-rotor BVI events are found on the advancing side of the lower rotor at $\alpha = -5°$, highly impulsive pressure pulses are expected at microphones on the port side. The same reasoning can be applied to explain the occurrence of impulsive pressure pulses at microphones on the starboard side of the $\alpha = 5°$ case. However, the pressure peaks are higher in magnitude on the port side as a consequence of stronger parallel rotor-to-rotor BVI events.

Mid-frequency sound pressure level (SPL), which is computed by integrating the SPL spectrum between 10th and 50th blade harmonics, is plotted (see Fig. 15) to show a better quantitative comparison. Both blade-crossover and BVI induced noise are included in mid-frequency SPL calculations. Again, the $\alpha = 5°$ case shows higher mid-frequency SPL at microphones positioned on the starboard side, while the $\alpha = -5°$ case shows higher peak values at microphones on the port side. The maximum differences between the $\alpha = -5°$ and 5° cases are found to be approximately 7 dB and 6 dB on the port and starboard sides, respectively. The mid-frequency SPL of the $\alpha = -5°$ case on the port side is higher than that of the $\alpha = 5°$ case on the starboard side. The acoustic results discussed in this section are also consistent with the aerodynamic results.

Decomposition of Rotor Acoustics at 150 Knots

For a detailed acoustic study, the loading noise acoustic pressure of the coaxial rotor is decomposed into two components at 150 knots: upper and lower rotors. Figure 16 shows a comparison of the loading noise acoustic pressure of the upper rotor. Again, the $\alpha = 5°$ case shows slightly higher magnitude of pressure peaks primarily on the starboard side due to the hub-wake interaction near $\Psi = 0°$ and parallel rotor-to-rotor BVI events near $\Psi = 45°$ and 90° of the upper rotor. Figure 17 shows a comparison of the loading noise acoustic pressure of the lower rotor. The $\alpha = -5°$ case shows higher pressure peaks on the port side also due to the impulsive parallel rotor-to-rotor BVI events in the first quadrant of the lower rotor and the intensive hub-wake interaction near $\Psi = 0°$.

Mid-frequency SPL is also computed for a quantitative comparison and shown in Fig. 18. According to Fig. 18a, the maximum difference between the $\alpha = -5°$ and 5° in mid-frequency SPL on the starboard side is approximately 6 dB. The maximum difference between the $\alpha = -5°$ and 5° in mid-frequency SPL on the port side is approximately 8 dB on the port side as shown in Fig. 18b. Overall, the $\alpha = -5°$ case shows higher mid-frequency SPL than the $\alpha = 5°$ case.

Acoustic Directivity at 150 Knots

The influence of pitch attitude on acoustic directivity is also studied at 150 knots. Acoustic simulations are performed on a hemispherical grid with the radius equal to 5R. 73 and 19 grid points are used in the azimuthal and latitudinal directions, respectively. Figure 19 shows the hemispherical plots from the top view for each case with the maximum and minimum mid-frequency SPL labeled on the colorbar. It should be noted that the maximum and minimum noise levels in the color bars are not the same for each plot. As α increases, mid-frequency

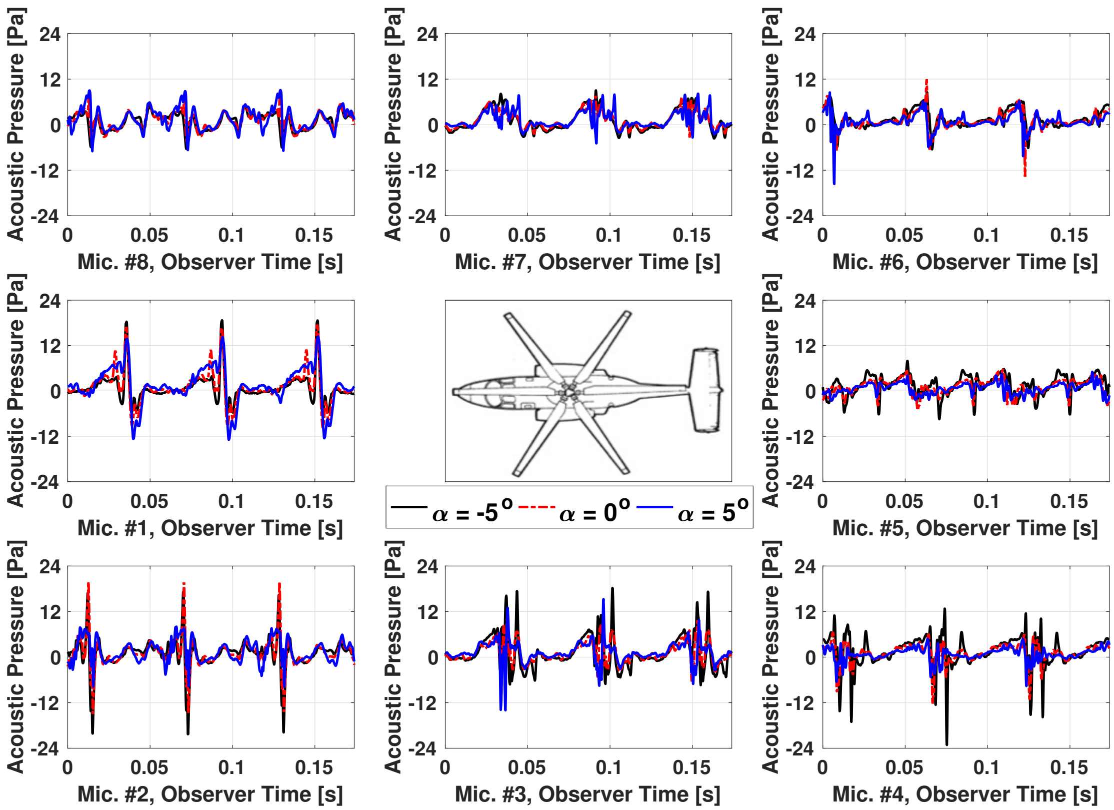

Fig. 14: Loading noise comparison at 150 knots.

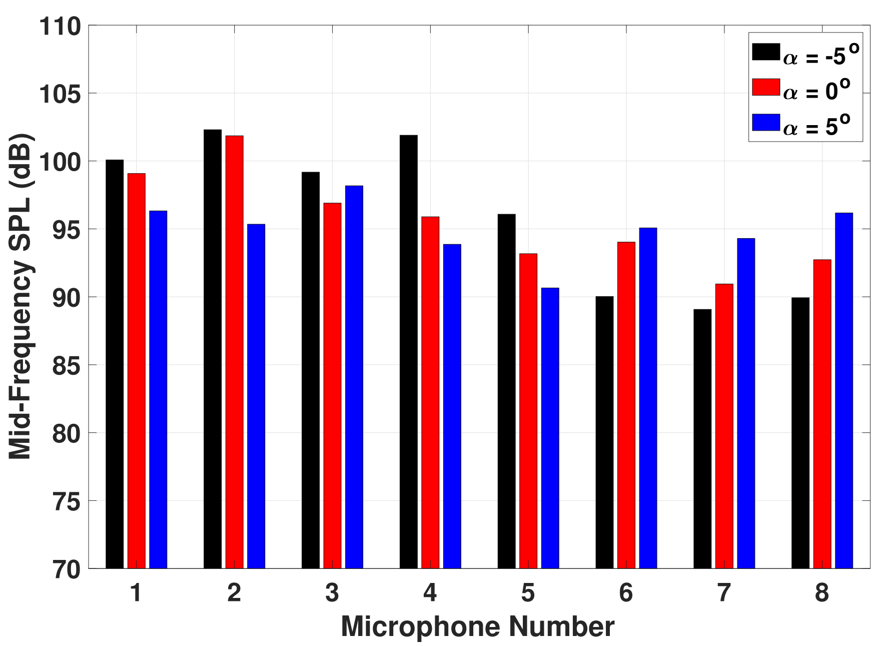

Fig. 15: Mid-frequency SPL comparison at 150 knots.

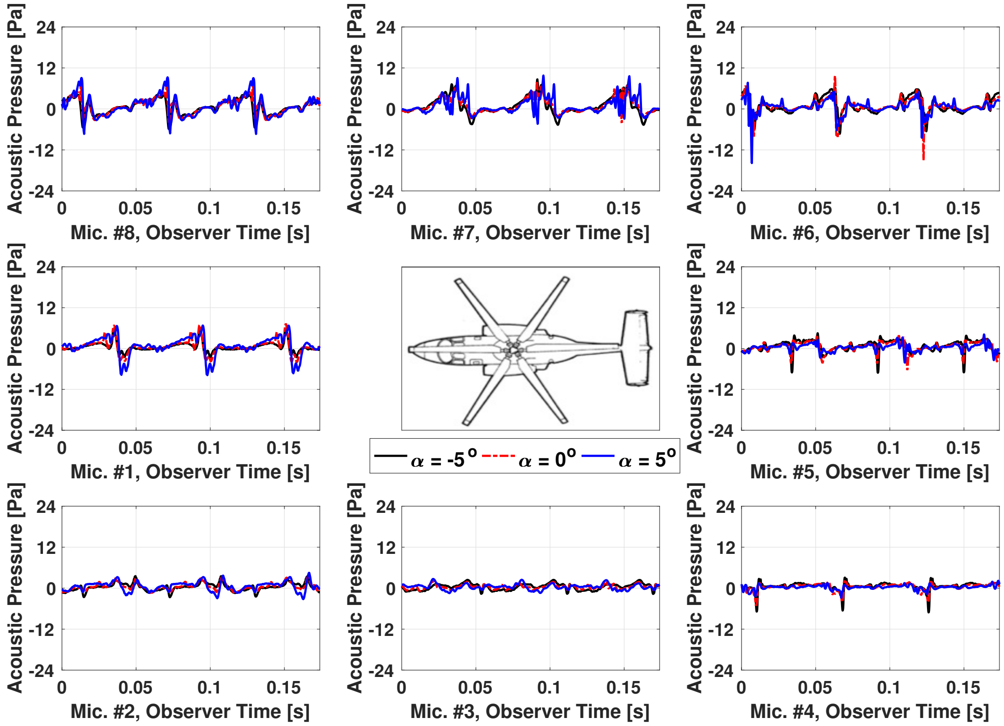

Fig. 16: A comparison of upper-rotor loading noise at 150 knots.

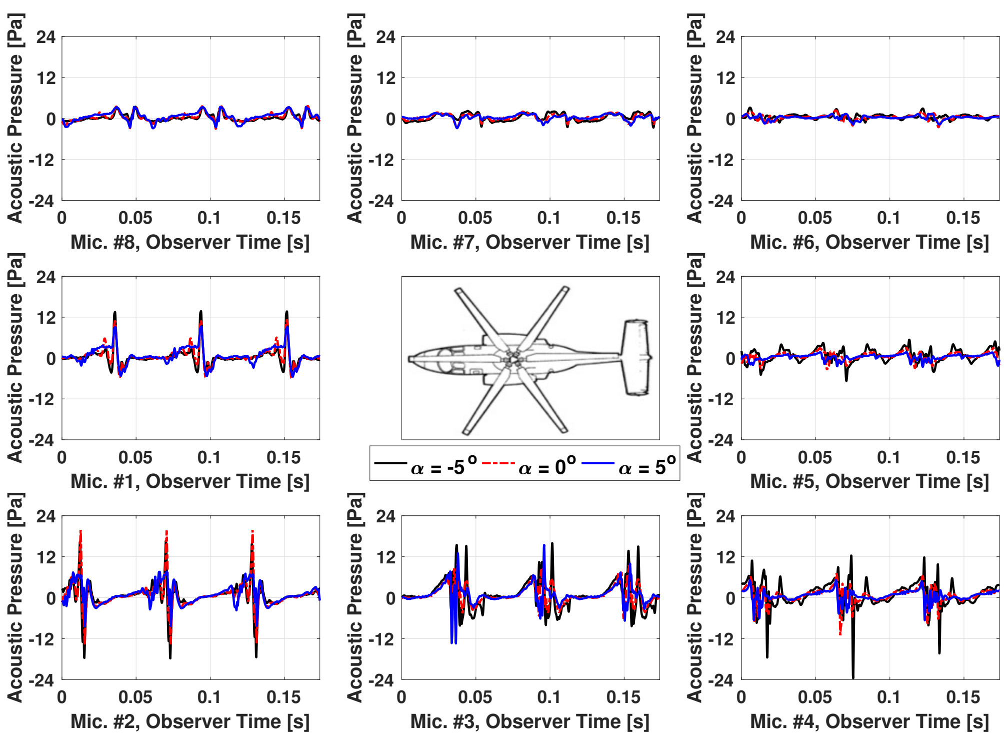

Fig. 17: A comparison of lower-rotor loading noise at 150 knots.

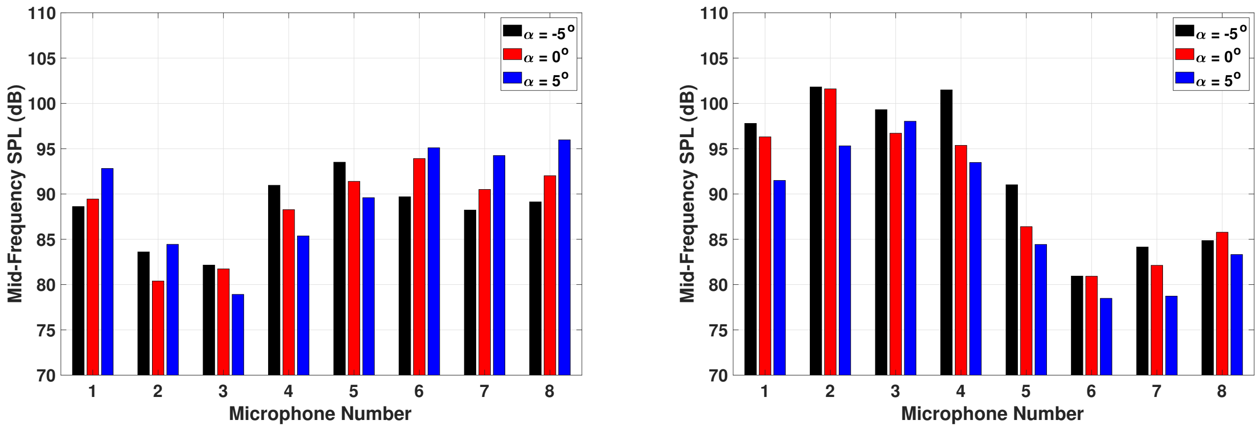

(a) Upper rotor. **(b) Lower rotor.**

Fig. 18: Rotor decomposition of mid-frequency SPL at 150 knots

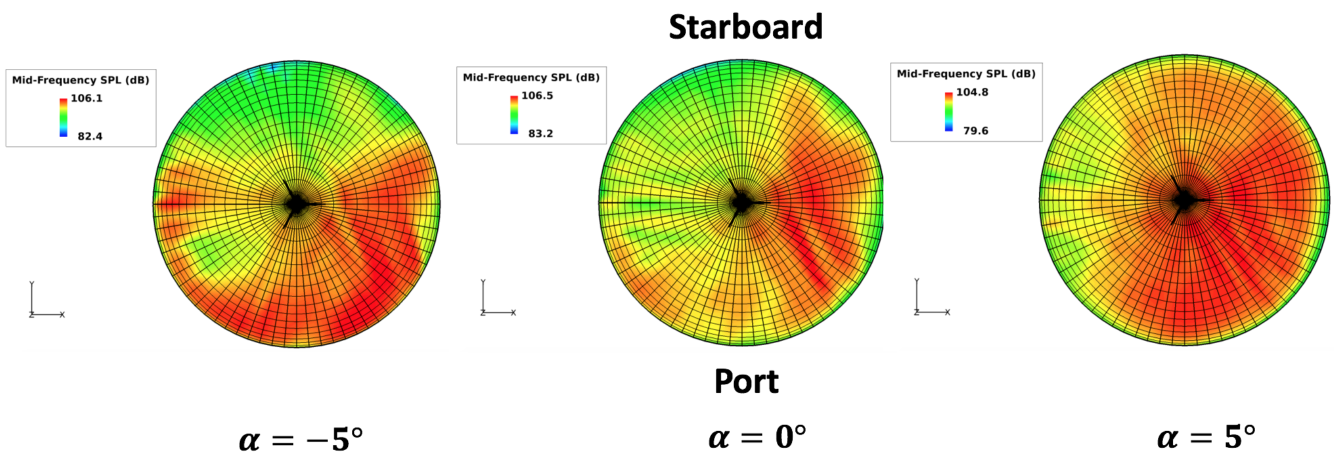

Fig. 19: Hemispherical-grid simulation at 150 knots.

SPL in the forward direction is reduced. On the contrary, mid-frequency SPL in the rear region is increased as α increases. Furthermore, the $\alpha = -5°$ case shows a bias distribution of mid-frequency SPL toward the port side of the coaxial rotor. The $\alpha = 5°$ case shows a more evenly distributed mid-frequency SPL map on both port and starboard sides in the rear region. The positive pitch attitude case has a clear noise advantage.

Acoustics at 200 Knots

Acoustic analysis is also performed at 200 knots ($\mu = 0.59$). Figure 20 shows the loading noise acoustic pressure of the three α cases at the eight microphone positions. Similar to the trend seen at 150 knots, the $\alpha = -5°$ case shows overall higher acoustic pressure peaks, especially at microphones positioned on the port side probably due to highly impulsive rotor-to-rotor BVIs. A detailed aerodynamic analysis at 200 knots will be pursued in future work in order to investigate the mechanism of noise source.

A comparison of mid-frequency SPL is also conducted at 200 knots and shown in Fig. 21. The $\alpha = -5°$ case shows dramatically higher mid-frequency SPL on the port side. The largest difference between the $\alpha = -5°$ and $5°$ cases is approximately 14 dB. Unlike the 150 knots speed case, the $\alpha = 0°$ case shows higher mid-frequency SPL than the $\alpha = 5°$ case on the port side, which is thought to be induced by the strong impulsive self-BVI event in the first quadrant of the upper rotor at $\alpha = 0°$ as found by Jia et al. (Ref. 15).

Power Performance and Rotor Aerodynamic Efficiency

Both power and rotor aerodynamic performance of the coaxial configuration are analyzed and correlated with rotor acoustics. The auxiliary propulsion power of the vehicle is estimated based on a propeller propulsive efficiency factor $\eta = 0.9$, which has also been assumed in the previous research (Refs. 6, 8, 15). The total power of the coaxial configuration is approximated using the following equation:

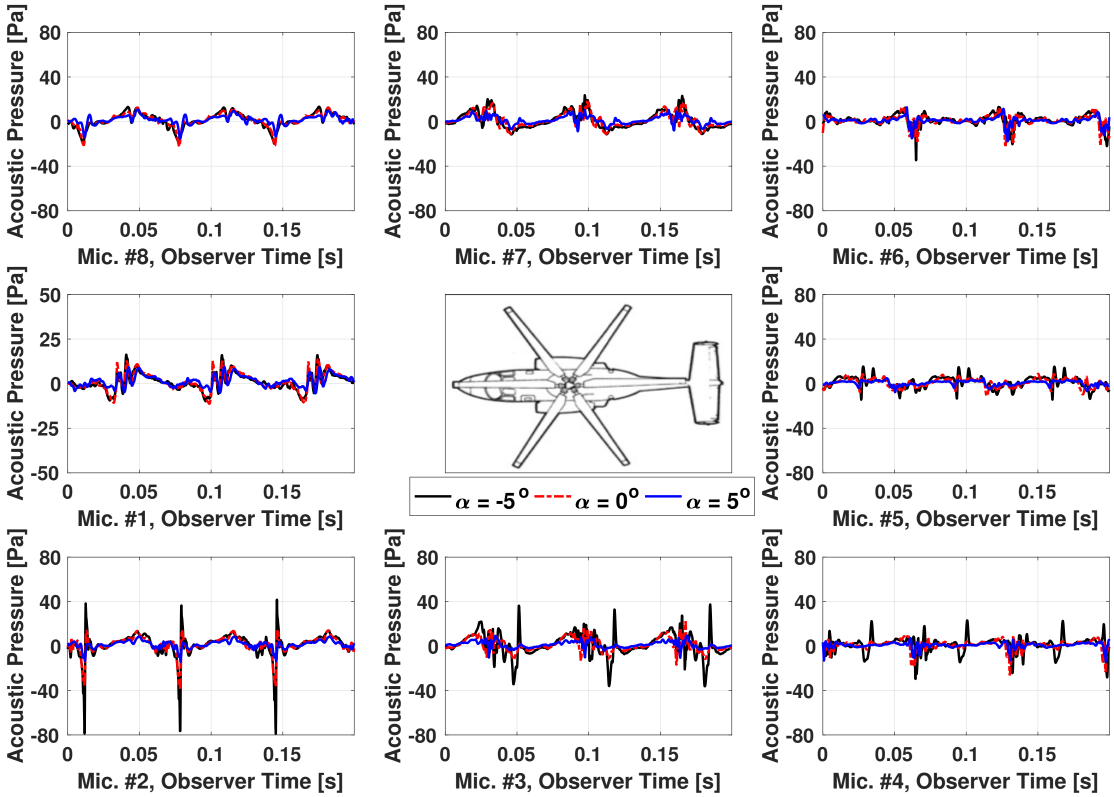

Fig. 20: Loading noise comparison at 200 knots.

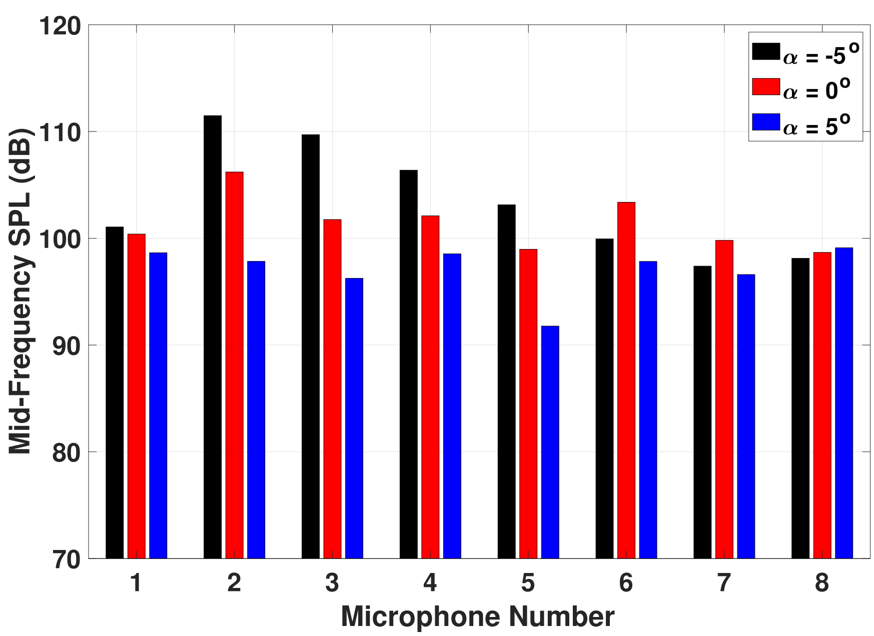

Fig. 21: Mid-frequency SPL comparison at 200 knots.

$$P_{total} = P_{upper} + P_{lower} + \frac{T_{aux} \cdot V_\infty}{\eta}, \quad (5)$$

where P_{total} is the total power, P_{upper} is the upper rotor power, P_{lower} is the lower rotor power, and T_{aux} is the thrust produced by auxiliary engines. The third term on the right hand side of Eq. (5) is the auxiliary propulsion power. Figure 22 shows a comparison of power performance at 150 and 200 knots. No significant difference in total power is found between the $\alpha = -5°$, $0°$, and $5°$ cases at 150 knots. However, the $\alpha = 5°$ case shows least rotor power when the coaxial rotor behaves similar to an autogiro, consuming less power in forward flight. Since the majority of propulsive force is not generated by the coaxial rotor at a positive α, the maximum auxiliary propulsion power is found at $\alpha = 5°$. As the flight speed increases from 150 to 200 knots, the trend becomes slightly different. The minimum total power is found at $\alpha = 5°$. It should be kept in mind that the rotor rotation rate is reduced from 100% (nominal condition) to 90% at 200 knots. This reduction in rotor rotation rate lowers the total rotor power of all cases. Recall Fig. 21, the $\alpha = 5°$ overall shows lower mid-frequency SPL than the other two cases at almost all microphone locations. Therefore, both power and acoustic performance of the vehicle can be improved by operating the vehicle at a slightly positive α.

The effective lift-to-drag ratio of the coaxial rotor (L/D_e) was also computed to evaluate the rotor aerodynamic efficiency. The equation of L/D_e is shown below:

$$\frac{L}{D_e} = \frac{L}{(P_{upper} + P_{lower})/V_\infty + D} \quad (6)$$

where L is the rotor lift and D is the rotor drag in the wind-axis direction. Johnson (Ref. 6) and Go et al. (Ref. 32) also computed L/D_e of a notional XH-59A model based on the same convention. Figure 23 shows a comparison of L/D_e between available flight test data (Ref. 6) and simulation results. Though the flight conditions such as α are not given in the reference, an α of $5°$ is assumed since most modern compound coaxial rotorcraft fly at a slightly positive α in high-speed forward flight. Overall, the simulation results are in good agreement with the flight test data, although the 150 knots case was slightly underpredicted. Figure 24 shows a comparison of L/D_e between the $\alpha = -5°$, $0°$, and $5°$ cases at 150 and 200 knots. The $\alpha = 5°$ case shows higher L/D_e than the other two cases, especially at 200 knots, and thus a positive α is recommended for high-speed cruise operations.

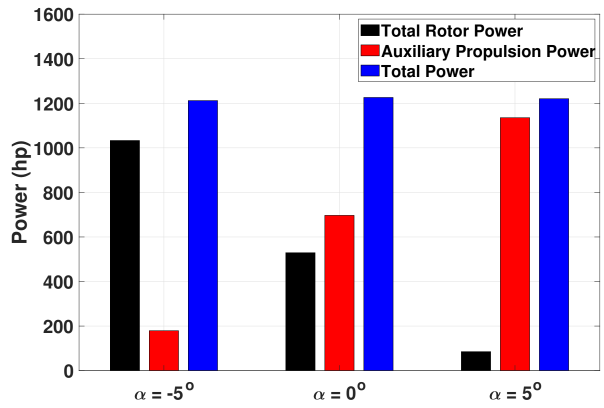

(a) 150 knots.

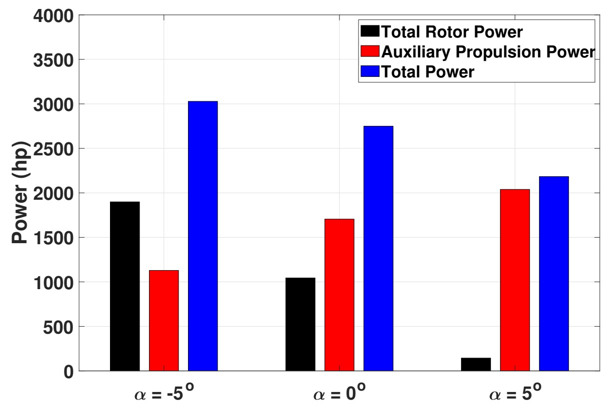

(b) 200 knots.

Fig. 22: Power performance at 150 and 200 knots

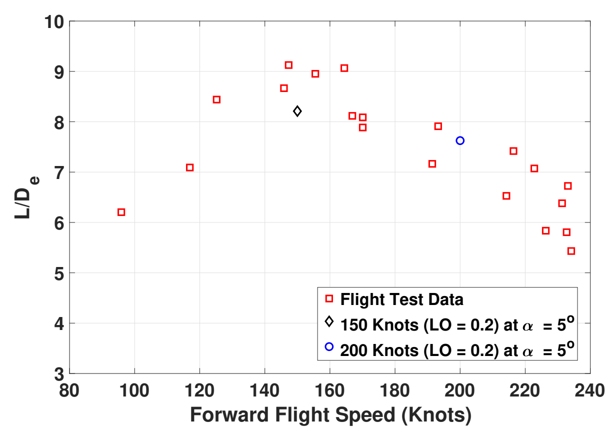

Fig. 23: Validation of rotor aerodynamic efficiency (L/D_e).

CONCLUSIONS

High-fidelity CFD/CSD loose coupling simulations have been performed to investigate the effect of pitch attitude on both performance and acoustics of a lift-offset coaxial rotor in high-speed forward light. The three pitch attitudes selected for this research were $-5°$, $0°$, and $5°$ at 150 and 200 knots. Acoustic simulations were performed based on an impermeable surface strategy at eight microphones positioned 1R below the coaxial rotor. In addition to the acoustic analysis, a detailed aerodynamic study was conducted at 150 knots to better understand the fundamental mechanism of acoustic sources as the pitch attitude varies. Both vehicle power and rotor aerodynamic efficiency were also analyzed and correlated with rotor acoustics. The following conclusions were drawn based on the results presented in this paper:

1. The hub-wake, self-BVI, parallel rotor-to-rotor BVI, blade-crossover, root-induced BVI, and reversed-flow-

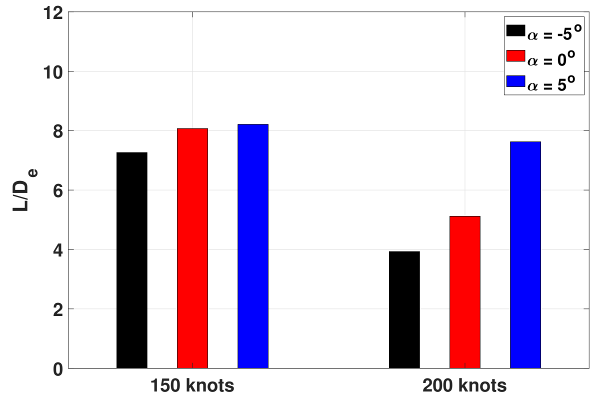

Fig. 24: Rotor aerodynamic efficiency (L/D_e) at 150 and 200 knots.

edge-vortex interactions are the major aerodynamic events of a lift-offset coaxial rotor in high-speed forward flight. The strength of these events is dependent on the pitch attitude. Although root-induced BVI interactions are non-physical aerodynamic interactions due to a gap placed between the blade and the hub fairing, the strength of these interactions are weak due to the viscous interaction of the hub.

2. The hub-wake interaction, which is merged with root-induced BVIs and reversed-flow-edge-vortex interactions, can be an intensive acoustic source of a coaxial rotor. The wake visualizations also showed that the hub wake interaction is also more likely to impact the upper rotor at a positive pitch attitude.

3. Parallel rotor-to-rotor BVIs are highly impulsive acoustic sources of a coaxial rotor under conditions in which the pitch attitude is negative due to a smaller separation distance between the tip vortex and blade surface. Even though parallel rotor-to-rotor BVIs are also present at a positive attitude, the strength is relatively weaker.

4. The strength of highly impulsive blade-crossover events is reduced at a positive pitch attitude due to weaker pressure interaction between the upper and lower rotor blades.

5. The lift-offset coaxial rotor generally showed higher mid-frequency SPL at a negative pitch attitude. The biggest difference in mid-frequency SPL between the positive and negative pitch attitude cases can be as large as 14 dB at 200 knots. According to the rotor acoustic decomposition, the lower rotor contributes significant contribution to loading noise at a negative pitch attitude, whereas the upper rotor contributes significantly to loading noise at a zero/positive pitch attitude.

6. Hemispherical acoustic simulations at 150 knots showed that the noise is less likely to propagate in the forward direction at a positive pitch attitude.

7. Significant improvement in rotor acoustics, rotor aerodynamic efficiency, and vehicle power performance can be gained by flying the vehicle at a slightly positive pitch attitude in high-speed forward flight.

A detailed aerodynamic analysis at 200 knots will be included in future work to identify potential impulsive noise sources. A comparison between hub and hubless simulations will also be conducted to investigate the effect of hub-wake interaction on rotor acoustics. Full vehicle simulations, which incorporate a pusher propeller to represent a modern lift-offset coaxial configuration, will be considered for future work. It is anticipated that both BVI trajectory and associated acoustics can be significantly different from isolated rotor simulations in the presence of a pusher propeller.

ACKNOWLEDGMENTS

This research was partially funded by the Government under Agreement No. W911W6-17-2-0003. The U.S. Government is authorized to reproduce and distribute reprints for Government purposes notwithstanding any copyright notation thereon. The views and conclusions contained in this document are those of the authors and should not be interpreted as representing the official policies, either expressed or implied, of the Aviation Development Directorate or the U.S Government.

The authors would like to sincerely thank: Dr. Roger Strawn from the U.S. Army Aviation Development Directorate (ADD) at Moffett Field, Mountain View, CA for providing invaluable DoD High Performance Computing (HPC) resources and summer internship for the fist author; the Helios team from ADD, especially Mark Potsdam, Jain Rohit, and Dr. Beatrice Roget, for their insightful advice on CFD/CSD modeling.

REFERENCES

[1]Hirschberg, M., "JMR Technology Demonstration Update: The Road to Future Vertical Lift," *Vertiflite*, Vol. 62, (1), Vertical Flight Society, Fairfax, VA, 2016, pp. 22–27.

[2]"SB>1 DEFIANT™ JMR Technology Demonstrator," Lockheed Martin, https://lockheedmartin.com/en-us/products/sb1-defiant-technology-demonstrator.html.

[3]Ruddell, A. J. and Marcrino, J. A., "Advancing Blade Concept (ABC) High Speed Development," American Helicopter Society 36th Annual Forum Proceedings, Washington, D.C., May 13–15, 1980.

[4]Burgess, R. K., "The ABC™ Rotor — A Historical Perspective," American Helicopter Society 60th Annual Forum Proceedings, Baltimore, MD, June 7–10, 2004.

[5]Walsh, D., Weiner, K., Arifian, K., Lawrence, T., Wilson, T., Millott, T., and Blackwell, R., "High Airspeed Testing of the Sikorsky X2 Technology™ Demonstrator," American Helicopter Society 67th Annual Forum Proceedings, Virginia Beach, VA, May 4, 2011.

[6]Johnson, W., "Influence of Lift Offset on Rotorcraft Performance," NASA TP-2009-215404, Nov. 2009.

[7]Yeo, H. and Johnson, W., "Investigation of Maximum Blade Loading Capability of Lift-Offset Rotors," American Helicopter Society 69th Annual Forum Proceedings, Phoenix, AZ, May 21–23, 2013.

[8]Jacobellis, G., Gandhi, F., and Floros, M., "A Physics-Based Approach to Trim Optimization of Coaxial Helicopters in High-Speed Flight," American Helicopter Society 71st Annual Forum Proceedings, Virginia Beach, VA, May 5–7, 2015.

[9]Herman, T. A., Celi, R., and Baeder, J. D., "Multidisciplinary Trim Analysis of a Coaxial-Pusher Rotorcraft Configuration," American Helicopter Society 74th Annual Forum Proceedings, Pheonix, AZ, May 14–17, 2018.

[10]Walsh, G., Brentner, S. B., Jacobellis, G., and Gandhi, F., "An Acoustic Investigation of Coaxial Helicopter in High-Speed Flight," American Helicopter Society 72nd Annual Forum Proceedings, West Palm Beach, FL, May 17–19, 2016.

[11]Saberi, H., Khoshlahjeh, M., Ormiston, R., and Rutkowski, M., "Overview of RCAS and Application to Advanced Rotorcraft Problems," AHS Fourth Decennial Specialists Conference on Aeromechanics, San Francisco, CA, Jan. 2004.

[12]Kim, H. W., Duraisamy, K., and Brown, R., "Aeroacoustics of a Coaxial Rotor in Level Flight," American Helicopter Society 64th Annual Forum Proceedings, Montréal, Canada, April 29 – May 1, 2008.

[13]Brown, R. E., "Rotor Wake Modeling for Flight Dynamic Simulation of Helicopters," *AIAA Journal*, Vol. 10, (2), Jan. 2000, pp. 57–63.

[14]Schatzman, N. L., Komerath, M., and Romander, E. A., "Time-Varying Loads of Co-Axial Rotor Blade Crossings," *SAE International Journal of Aerospace*, Vol. 10, (2), Dec. 2017.

[15]Jia, Z., Lee, S., Sharma, K., and Brentner K. S., "Aeroacoustic Analysis of a Lift-Offset Coaxial Rotor Using High-Fidelity CFD-CSD Loose Coupling Simulation," American Helicopter Society 74th Annual Forum Proceedings, Pheonix, AZ, May 14–17, 2018.

[16]Jia, Z., Lee, S., and Brentner K. S., "Assessment of Turbulence Modeling and Wake-Grid Resolution for Lift-Offset Coaxial Rotor Simulations," AIAA 2018-4120, 36th AIAA Applied Aerodynamics Conference, Atlanta, GA, June 25–29, 2018.

[17]Ruddell, A. J., "Advancing Blade Concept (ABC) Technology Demonstrator," Technical Report USAAVRADCOM-TR-81-D-35, U.S. Army Research and Technology Laboratories (AVRADCOM), Apr. 1981.

[18]Chan, W. M., Rogers, S. E., Pandya, S. A., Kao, D. L., Buning, P. G., Meakin, R. L., Boger, D. A., and Nash, S. M., *Chimera Grid Tools User's Manual*, V. 2.1, NASA Ames Research Center, Moffett Field, CA, Mar. 2010.

[19]Wissink, A., Potsdam, M., Jain, R., Leffell, J., Jayaraman, B., Roget, B., Lakshminaravan, V., Forsythe, J., Sitaraman, J., and Bauer, A., "Improvements in the Helios Rotorcraft Simulation Code," American Helicopter Society 72nd Annual Forum Proceedings, West Palm Beach, FL, May 17–19, 2016.

[20]Felker III, F. F., "Performance and Loads Data from a Wind Tunnel Test of a Full-Scale, Coaxial, Hingeless Rotor Helicopter," NASA-TM-81329, Oct. 1981.

[21]Nichols, R., Tramel, R., and Buning, P., "Solver and Turbulence Model Upgrades to OVERFLOW 2 for Unsteady and High-Speed Flow Applications," AIAA 25th Applied Aerodynamics Conference, San Francisco, CA, June 5–8, 2006.

[22]Wissink, A. M., Kamkar, S., Pulliam, T., Sitaraman, J., and Sankaran, V., "Cartesian Adaptive Mesh Refinement for Rotorcraft Wake Resolution," AIAA Paper 2010-4554, 28th AIAA Applied Aerodynamics Conference, Chicago, IL, June 28 –July 1, 2010.

[23]Spalart, P. R. and Allmaras, S. R., "A One-Equation Turbulence Model for Aerodynamics Flows," AIAA 92-0439, 30th Aerospace Sciences Meeting and Exhibit, Reno, NV, Jan. 6–9, 1992.

[24]Spalart, P. R., Deck, S., Shur, M. L., Squires, K. D., Strelets, M. K., and Travin, A., "A New Version of Detached-Eddy Simulation, Resistant to Ambiguous Grid Densities," *Theoretical and Computational Fluid Dynamics*, Vol. 20, (3), July 1, 2006, pp. 181–195.

[25]Potsdam, M., Yeo, Hyeonsoo, and Johnson, W., "Rotor Airloads Prediction Using Loose Aerodynamic/Structural Coupling," *Journal of Aircraft*, Vol. 43, (3), May–June 2006, pp. 732–742.

[26]Brentner, K. S., Brès, G. A., Perez, G., and Jones, H. E., "Maneuvering Rotorcraft Noise Prediction: A New Code for a New Problem," American Helicopter Society Aerodynamics, Acoustics, and Test and Evaluation Technical Specialist Meeting, San Francisco, CA, Jan. 13–25, 2002.

[27]Lee, S., Brentner, K. S., Farassat, F., and Morris, P. J., "Analytic Formulation and Numerical Implementation of an Acoustic Pressure Gradient Prediction," *Journal of Sound and Vibration*, Vol. 319, (3-5), Jan. 2009, pp. 1200–1221.

[28]Brentner, K. S. and Farassat, F., "Modeling Aerodynamically Generated Sound of Helicopter Rotors," *Progress in Aerospace Sciences*, Vol. 39, (2-3), Feb.–Apr. 2003, pp. 83–120.

[29]Farassat, F. and Succi, G. P., "The Prediction of Helicopter Discrete Frequency Noise," *Vertica*, Vol. 7, (4), 1983, pp. 309–320.

[30]Ffowcs Williams, J. E. and Hawkings, D. L., "Sound Generation by Turbulence and Surface in Arbitrary Motion," *Philosophical Transactions of the Loyal Society*, London, United Kingdom, Series A, Vol. 264, (1151), May 1969, pp. 321–342.

[31]Potsdam, M., Datta, A., and Jayaraman, B., "Computational Investigation and Fundamental Understanding of a Slowed UH-60A Rotor at High Advance Ratios," *Journal of the American Helicopter Society*, Vol. 61, (2), Apr. 2016, pp. 1–17.

[32]Go J., Kim, D., and Park, J., "Performance and Vibration Analyses of Lift-Offset Helicopters," *International Journal of Aerospace Engineering*, Article ID 1865751, Vol. 2017, June 2017.